Progress In Electromagnetics Research C, Vol. 172, 79–88, 2026

PIER C

(Received 1 June 2026, Accepted 6 July 2026, Scheduled 31 July 2026)

Research on Vibration Suppression of Flux-Switching Permanent Magnet Machine

Libing Jing, Longxiang Han, Yeming Zhu, Mingji Yin, Yuhui Huang, and Zeyu Min*

China Three Gorges University, China

ABSTRACT: To address vibration and noise issues in outer-rotor flux-switching permanent-magnet (OR-FSPM) machines for high-precision applications, radially magnetized PMs are placed between regular tangentially magnetized PMs, forming a U-shaped structure. An air-gap magnetic barrier is introduced between the two types of PMs to achieve magnetic isolation. Then, the spatiotemporal distribution of radial electromagnetic force density (EFD) waves is derived based on the magnetomotive force permeance model. Modal and harmonic response analyses are then conducted for both the conventional and proposed U-shaped machine topologies using electromagnetic-structural field simulations to reveal vibrational characteristics. The results demonstrate that the proposed U-shaped topology effectively suppresses second-order resonance while maintaining superior electromagnetic performance.

1. INTRODUCTION

The global energy transition and rapid evolution of electric vehicle (EV) technologies are placing ever-increasing demands on electric powertrain systems, necessitating higher power densities, superior efficiencies, and enhanced reliability [1]. Among various machine designs, the outer-rotor flux-switching permanent-magnet (OR-FSPM) machine has emerged as a promising candidate for direct-drive applications [2]. Similar to the conventional FSPM machine, the OR-FSPM machine features salient rotor teeth and Spoke-type PMs that produce a strong flux-focusing effect in the air gap. The corresponding analytical equations for back-EMF have been derived, confirming a highly sinusoidal back-EMF waveform [3]. Meanwhile, a simple rotor structure offers significant manufacturing advantages [4].

Although this field modulation mechanism contributes to improved machine performance, it inevitably introduces significant cogging torque and resultant torque ripple, adversely affecting system smoothness and increasing acoustic noise [5].

To address this challenge, extensive research efforts have been dedicated to electromagnetic design, structural parameter optimization, and advanced control strategies, with a particular focus on electromagnetic design and structural parameter optimization [6]. The key methods include cogging harmonic suppression via rotor tooth notching and skewing techniques [7], and the electromagnetic optimization design of stator pole arc and pole shoe geometries [8], the cooperative modulation of the PM position and magnetization direction [9, 10], and multi-objective collaborative design frameworks incorporating intelligent optimization algorithms [11, 12]. According to field-modulation theory, parallel magnetic circuits with radially magnetized PMs arranged in the stator teeth enhance working harmonics while suppressing non-working harmonics, thereby improving torque performance [13–15]. Additionally, some studies also combine flux-barrier and dual-PM effects to alleviate the flux-barrier effect and reduce torque ripple [16].

Most of the above suppression techniques are based on finite element methods. Analytical cogging torque expressions for field-modulated machines with different magnetization patterns have been derived using magnetic co-energy and permeance methods [17]. On this basis, tiny gaps are introduced between adjacent PMs, and the expression is derived for optimal gap sizing to minimize cogging torque [18].

In addition to electromagnetic performance, vibration and noise serve as critical indicators for evaluating machine performance and reliability [19, 20]. Electromagnetic vibration in field-modulated machines, such as OR-FSPM, presents a significant challenge, stemming predominantly from electromagnetic force density (EFD) waves in the air gap. These force waves act at the stator-rotor interface, exciting not only structural vibrations but also radiated acoustic noise. When the frequency of a dominant radial force wave coincides with the structural natural frequency, a condition known as resonance, the resultant amplification can significantly elevate vibration and noise levels, thereby compromising long-term operational stability [21].

Although substantial progress has been made in the electromagnetic design of OR-FSPM machines, a systematic investigation of their vibration characteristics remains insufficient, particularly regarding spatial and temporal distributions of the EFD and its underlying impact mechanisms.

To address this research gap, this study conducts a comprehensive analysis of radial EFD and vibration characteristics of an OR-FSPM machine. First, analytical expressions for the radial EFD are derived using the magnetomotive force permeance method to elucidate the origins of its spatiotemporal distribution. Second, spatiotemporal distributions of the air-gap flux

* Corresponding author: Zeyu Min (minzeyu@ctgu.edu.cn).

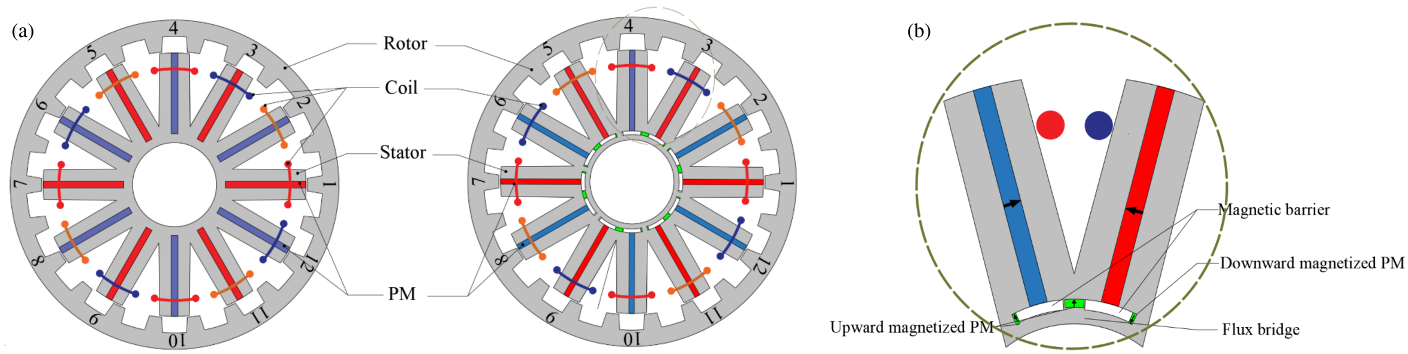

FIGURE 1. The topology. (a) Conventional and proposed machines and (b) partial enlarged PM structure of the proposed machine.

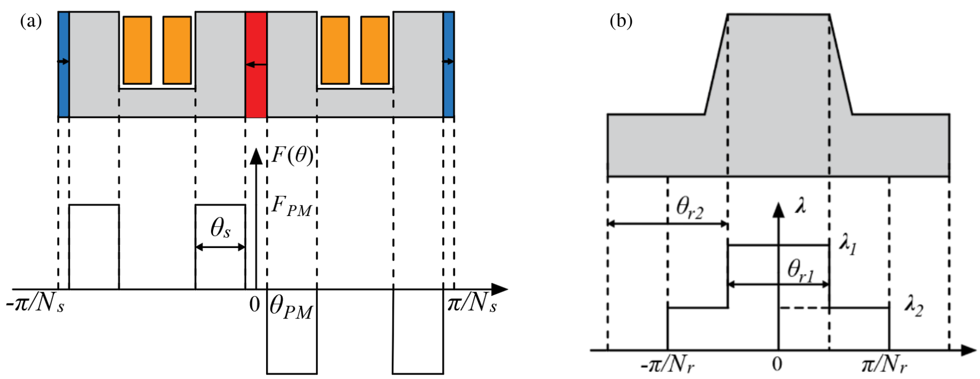

FIGURE 2. No-load analytical model. (a) Magnetomotive force of PM and (b) rotor permeability.

density and radial EFD are acquired via finite element (FE) simulations. Finally, a harmonic response analysis is performed by coupling the FE model with a three-dimensional (3D) structural model to investigate the vibrational behavior of the machine.

2. PROPOSED TOPOLOGY AND OPERATION PRINCIPLE

The configuration of the investigated OR-FSPM machines is illustrated in Fig. 1, with the specific parameters listed in Table 1. To improve electromagnetic performance, the proposed U-shaped OR-FSPM machine uses the conventional machine as a baseline and introduces two key modifications: an auxiliary air gap and radially magnetized PMs that complement inherent tangentially magnetized PMs. This arrangement effectively intensifies the flux concentration effect, resulting in a marked increase in air-gap flux density.

2.1. Calculation of the Air-Gap Magnetic Field

To systematically investigate vibration's electromagnetic origins, this section establishes analytical models for the air-gap flux density under both no-load and armature conditions.

These models serve as the foundation for subsequent force-harmonic derivation and structural response evaluation.

First, PM magnetomotive force (MMF) is characterized under no-load conditions. For analytical tractability, the PM MMF is approximated as a rectangular waveform distributed along the circumference, as illustrated in Fig. 2(a).

TABLE 1. Machine parameters.

Parameters	Value
Rated speed n_r (r/min)	800
Stator number N_s	12
Rotor number N_r	22
Rated power P_{out} (kW)	2
Air gap length g (mm)	0.7
No. of turn per phase n_{ph}	55
Outer radius of Stator R_{so} (mm)	70.1
Outer radius of Rotor R_{ro} (mm)	87.6
Rated Current I (A)	10
Axial length l_α (mm)	55
PM material	NdFeB
Iron material	DW315-50

In this model, F_{PM} denotes the peak MMF produced by PMs. The space position angle of the rotor is θ. θ_{PM} defines the half-arc length of each PM. The air gap MMF waveform, $F_{PMg}(\theta)$, is expressed as a rectangular function whose Fourier series is:

$$\begin{cases} F_{PMg}(\theta) = \dfrac{4F_{PM}}{\pi} \displaystyle\sum_{\mu=1,3,5\ldots}^{\infty} F_{PM\mu} \sin(\mu P_s \theta) \\ F_{PM\mu} = \dfrac{\cos \mu P_s \theta_s - \cos \mu P_s \theta_{PM}}{\mu} \end{cases} \tag{1}$$

where μ denotes a positive odd integer, and $P_s = N_s/2$ represents the number of PM pole pairs, which is six. Rotor saliency modulates the air-gap permeance, which is characterized by a periodic permeance function $\lambda(\theta, t)$, as illustrated in Fig. 2(b) and is expressed as follows:

$$\begin{cases} \lambda(\theta,t) = \dfrac{\lambda_0}{2} + \displaystyle\sum_{k=1}^{\infty} \lambda_k \cos(kN_r(\theta - \omega_r t - \theta_0)) \\ \lambda_0 = \dfrac{N_r}{\pi}(\theta_{r1}\lambda_1 - \theta_{r2}\lambda_2) \\ \lambda_k = \dfrac{2(\lambda_1 - \lambda_2)\sin(kN_r \frac{\theta_{r2}}{2})}{k\pi} \end{cases} \tag{2}$$

where λ_0 and λ_2 are the maximum permeances over a tooth and a slot, respectively; k is any positive integer; and ω_r and θ_0 are the rotor speed and initial angle, respectively.

Under no-load conditions, the radial air-gap flux density $B_{mag}(\theta, t)$ is obtained by multiplying the PM MMF by air-gap permeance as follows:

$$\begin{aligned} B_{mag}(\theta,t) =& F_{PMg}(\theta) \cdot \lambda(\theta,t) \\ =& \frac{2F_{PM}\lambda_0}{\pi} \sum_{\mu=1,3,5\ldots}^{\infty} F_{PM\mu} \sin(\mu P_s \theta) + \\ & \frac{2F_{PM}}{\pi} \sum_{\mu=1,3,5\ldots}^{\infty} \sum_{k=1}^{\infty} F_{PM\mu} \lambda_k \sin(\beta_1 + \beta_2) \end{aligned} \tag{3}$$

where

$$\begin{cases} \beta_1 = (\mu P_s + kN_r)\left(\theta - \dfrac{kN_r\omega_r t + kN_r\theta_0}{\mu P_s + kN_r}\right) \\ \beta_2 = (\mu P_s - kN_r)\left(\theta + \dfrac{kN_r\omega_r t + kN_r\theta_0}{\mu P_s - kN_r}\right) \end{cases} \tag{4}$$

Under load, the armature-reaction field must be superimposed. The stator carries non-overlapping concentrated windings whose phase vectors are shown in Fig. 3.

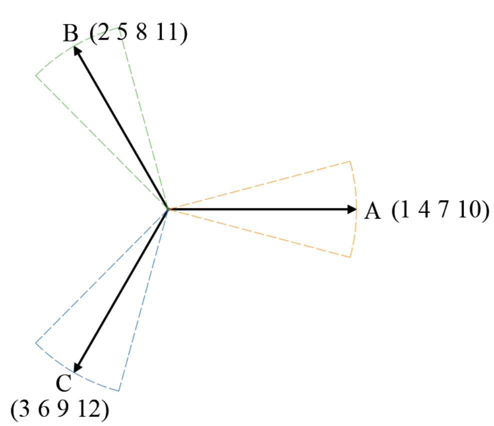

FIGURE 3. Winding-vector distribution of OR-FSPM machine.

With balanced three-phase excitation, the phase currents i_A, i_B, and i_C can be expressed as:

$$\begin{cases} i_A = \sqrt{2}I_{rm}\sin(\omega_e t) \\ i_B = \sqrt{2}I_{rm}\sin\left(\omega_e t - \dfrac{2\pi}{3}\right) \\ i_C = \sqrt{2}I_{rm}\sin\left(\omega_e t + \dfrac{2\pi}{3}\right) \end{cases} \tag{5}$$

where I_{rm} is the peak rated current, and $\omega_e = N_r\omega_r$ is the electrical angular frequency. Spatially combining the three-phase MMFs yields the resultant armature-reaction MMF $F(\theta, t)$:

$$F(\theta,t) = \frac{3}{2} \sum_{\nu=1,2,3\ldots}^{\infty} F_{\Phi\nu} \sin(\omega_e t - \nu\theta) \tag{6}$$

where

$$F_{\Phi\nu} = \frac{2\sqrt{2}}{\pi\nu} N_c k_{N1} I_{rms} \approx \frac{0.9N_c k_{N1} I_{rms}}{\nu} \tag{7}$$

where N_c is the number of winding turns, and k_{N1} is the winding factor.

The armature-reaction flux density $B_{arm}(\theta, t)$ follows from the product of the armature MMF and air-gap permeance:

$$\begin{aligned} B_{arm}(\theta,t) = F(\theta) \cdot \lambda(\theta,t) = \frac{3\lambda_0}{4} \sum_{\nu=1,2,3\ldots}^{\infty} F_{\Phi\nu} \sin(\omega_e t - \nu\theta) \\ + \frac{3}{4} \sum_{\nu=1,2,3\ldots}^{\infty} \sum_{k=1}^{\infty} F_{\Phi\nu} \lambda_k (\sin\beta_3 - \sin\beta_4) \end{aligned} \tag{8}$$

where

$$\begin{cases} \beta_3 = (kN_r - v)(\theta - \dfrac{(k-1)N_r\omega_r t + kN_r\theta_0}{kN_r - v}) \\ \beta_4 = (kN_r + v)(\theta - \dfrac{(k+1)N_r\omega_r t + kN_r\theta_0}{kN_r + v} \end{cases} \tag{9}$$

Using linear superposition, the resultant radial flux density under load $B_r(\theta, t)$ is expressed:

$$B_r(\theta,t) = B_{mag}(\theta,t) + B_{arm}(\theta,t) \tag{10}$$

The electromagnetic forces originate from the air-gap field. By using the Maxwell stress tensor and neglecting the tangential component on the rotor tooth surface, the radial EFD f_r can be approximated as follows:

$$f_r = \frac{1}{2\mu_0}(B_r^2 - B_t^2) \approx \frac{1}{2\mu_0}B_r^2 = \frac{1}{2\mu_0}(B_{mag} + B_{arm})^2 \tag{11}$$

where B_r and B_t are the radial and tangential components at the air gap, respectively, and μ_0 is the permeability of vacuum. The detailed solution process is not repeated, and the components of the OR-FSPM's radial EFD are obtained, as shown in Table 2.

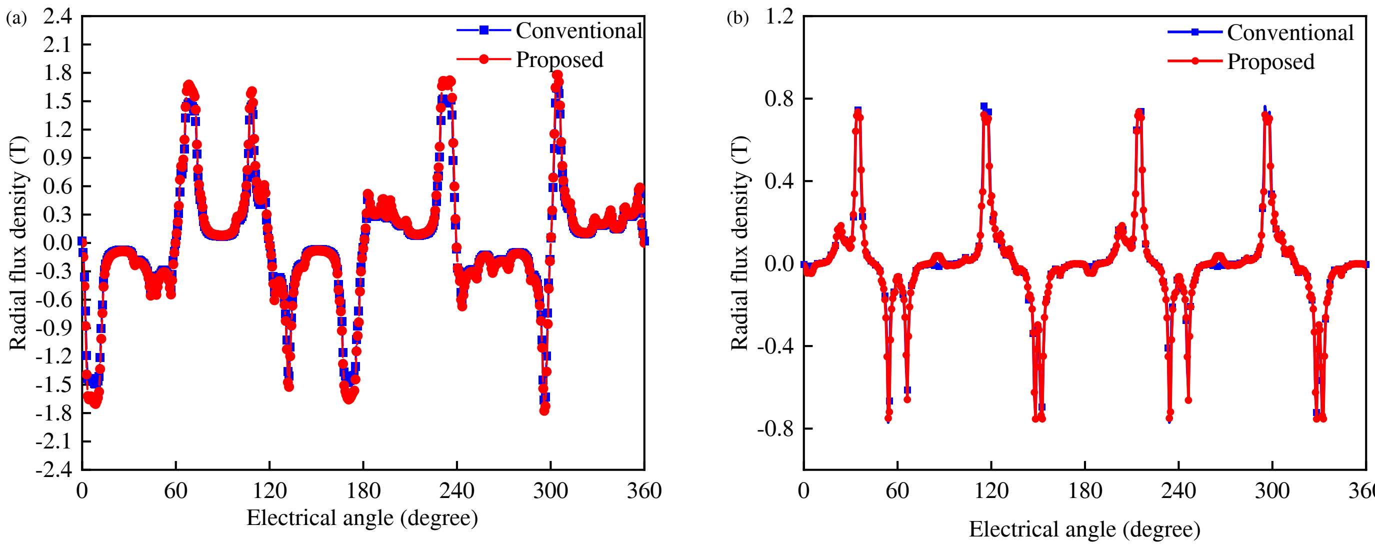

FIGURE 4. Flux density distribution. (a) No load condition and (b) armature condition.

TABLE 2. Components of electromagnetic force.

	Spatial order$r$	Time frequency	Amplitude
1	$(\mu_1 \pm \mu_2)P_s$	0	$\frac{2F_{PM}^2\lambda_0^2}{\pi^2}F_{PM\mu_1}F_{PM\mu_2}$
2	$kN_r \pm (\mu_1 \pm \mu_2)P_s$	kf	$\frac{4F_{PM}^2\lambda_0\lambda_k}{\pi^2}F_{PM\mu_1}F_{PM\mu_2}$
3	$(k_1 \pm k_2)N_r \pm (\mu_1 \pm \mu_2)P_s$	$(k_1 \pm k_2)f$	$\frac{2F_{PM}^2\lambda_{k_1}\lambda_{k_2}}{\pi^2}F_{PM\mu_1}F_{PM\mu_2}$
4	$-(v_1 \pm v_2)$	$(1 \pm 1)f$	$\frac{9\lambda_0^2}{16}$
5	$kN_r \pm^1 (v_1 \pm^2 v_2)$	$(k \pm^1 1 \pm^2 1)f$	$\frac{9\lambda_0}{16}F_{\phi 1}F_{\phi_2}\lambda_k$
6	$(k_1 \pm^1 k_2)N_r \pm^2 (v_1 \pm^1 v_2)$	$(k_1 \pm^2 1) \pm^1 (k_2 \pm^3 1)f$	$\frac{9\lambda_0}{32}F_{\phi 1}F_{\phi_2}\lambda_{k_1}\lambda_{k2}$
7	$\mu P_s \pm v$	vf	$\frac{3F_{PM}\lambda_0^2}{\pi}F_{PM\mu}F_{\Phi\nu}$
8	$\mu P_s \pm v \pm kN_r$	$(k \pm 1)f$	$\frac{3F_{PM}\lambda_0}{2\pi}\lambda_k F_{PM\mu}F_{\Phi\nu}$
9	$\mu P_s \pm (k_{1+}k_2)N_r \pm v$	$(k_1 \pm k_2 \pm 1)f$	$\frac{3}{4}\sum_{\nu=1,2,3\ldots}^{\infty}\sum_{k=1}^{\infty}F_{\Phi\nu}\lambda_k^2 F_{PM\mu}$

Note: f denotes the fundamental frequency of the machine.

2.2. Simulation and Analysis of Electromagnetic Performance of the Machine

The electromagnetic characteristics are evaluated via FE simulations, where a circular contour in the mid-air-gap plane is used to sample the radial flux density on the rotor surface. Fig. 4 compares the radial air-gap flux density of the proposed and conventional machines. The proposed machine exhibits a higher amplitude under no-load conditions. Fig. 5 presents the corresponding harmonic spectra. As shown in Fig. 5(a), the rotating working harmonics of orders 4, 8, 16, 28, and 30 generated by rotor-tooth modulation, together with stationary harmonics of orders 6 and 18 from the PMs, are all higher in the proposed machine, which contributes to the improvement. Under armature conditions, the harmonic amplitudes remain essentially unchanged, as the stator core modification of the proposed machine has limited influence on the armature-reaction flux path.

The radial EFD acting on the inner surface of the rotor is calculated using Equation (11). A 3D view of the improved air-gap radial EFD under no-load conditions, along with space-time harmonics, is shown in Fig. 6.

According to the machine parameters used in this paper ($N_r = 22$, $P_s = 6$), the radial EFD generated by the OR-FSPM machine in a no-load state can be expressed as $|uN_r \pm 2vP_s|$, and the corresponding frequency is $uN\omega$, where u and v are integers, such as 0, ± 1, ± 2 .... The main low-order force wave components generated by the PM magnetic field are summarized in the first three rows of Table 3. These low-order harmonics have a significant impact on machine vibration [22].

A comparison between the FE results, presented in Fig. 6, and the analytical predictions confirms the consistency of the main force-wave components in terms of both spatial order and frequency. The results successfully verify correctness of the theoretical model and provide a reliable foundation for subsequent vibration response analysis.

Under armature reaction, the air-gap field distribution is markedly reshaped, yielding a denser and more complex radial-force spectrum, as shown in Fig. 7. However, the electromagnetic force and spatiotemporal harmonic distributions un-

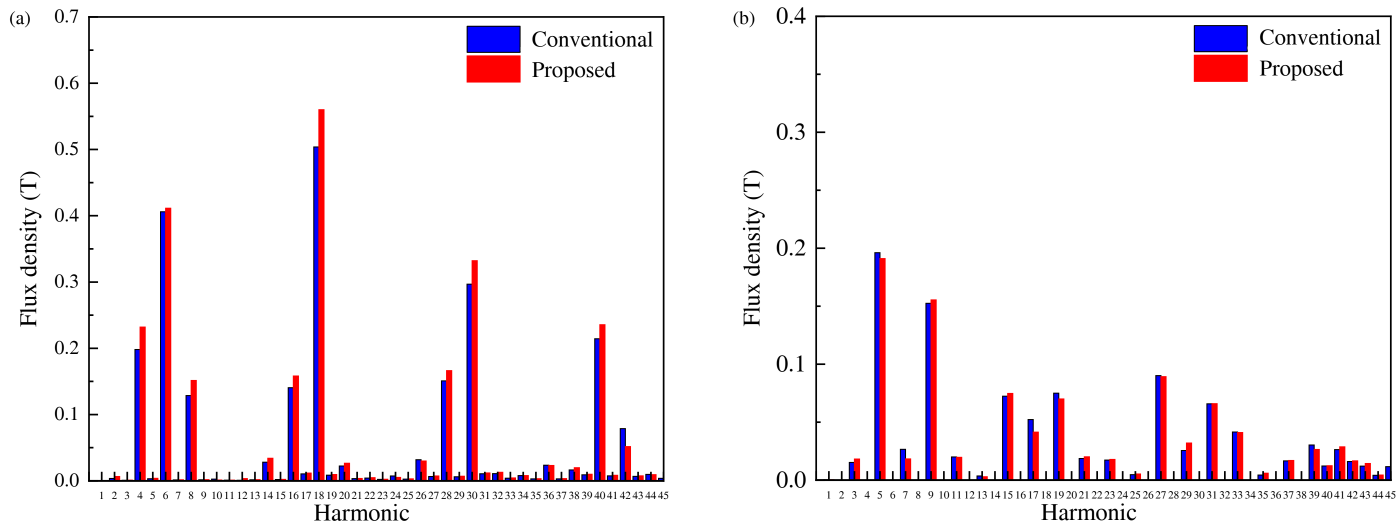

FIGURE 5. Harmonic spectra. (a) No load condition and (b) armature condition.

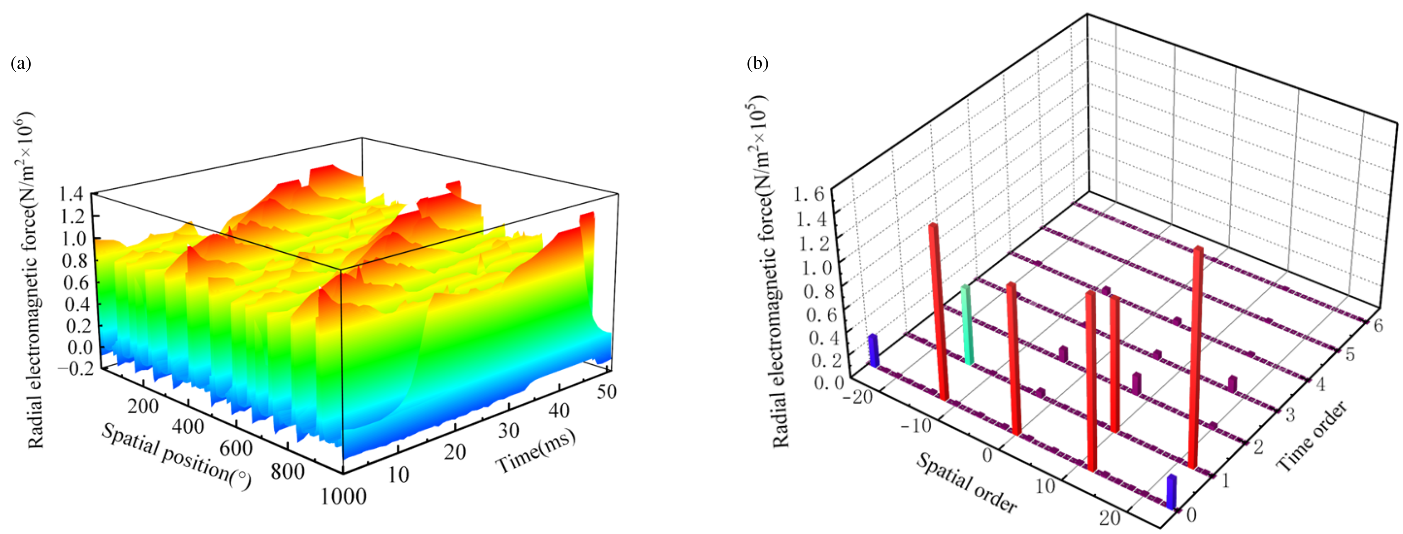

FIGURE 6. Radial EFD and space-time harmonics under no-load condition. (a) Radial EFD, (b) space-time harmonics.

TABLE 3. Radial EFD generated by no-load conditions.

u \ v	0	1	2	3
0	$(0, 0)$	$(22, f)$	$(44, 2f)$	$(66, 3f)$
1	$(-12, 0)$ $(12, 0)$	$(10, f)$ $(34, f)$	$(32, 2f)$ $(56, 2f)$	$(54, 3f)$
2	$(24, 0)$ $(-24, 0)$	$(-2, f)$ $(46, f)$	$(20, 2f)$ $(68, 2f)$	$(42, 3f)$
3	$(36, 0)$ $(-36, 0)$	$(-12, f)$ $(58, f)$	$(8, 2f)$	$(30, 3f)$
4				$(18, 3f)$

der this condition are one order of magnitude lower than those under no-load operation.

Several new harmonics emerge in the radial electromagnetic force distribution, notably $(-20, f)$, $(-8, f)$, and $(15, f)$, corresponding to $(v_1 = 2, v_2 = 0, k_1 = 0, k_2 = 1)$, $(v_1 = 2, v_2 = 3, k = 1)$, and $(v_1 = 3, v_2 = 4, k_1 = 1, k_2 = 0)$, respectively. Other harmonics can also be analyzed similarly, although the amplitude under armature conditions is greatly reduced.

The interaction between the PM and armature fields generates complex spatiotemporal harmonics in the radial force, with the complete distribution shown in Fig. 8. Notably, when the temporal order is 2 and the spatial order -4, the amplitude of the radial EFD is relatively large. The proposed machine introduces no new dominant spatial harmonics yet significantly alters their amplitudes.

Figure 9 compares the spatial harmonic distributions of the radial EFD at the second temporal order. According to mechanical impedance theory, the vibration displacement is proportional to the EFD amplitude but inversely proportional to the square of its spatial order [23]. Hence, the -4th harmonic, characterized by a low spatial order and high amplitude, is of particular concern. In the proposed machine, the 4th radial EFD decreases from 40.36 kN/m^2 to 32.15 kN/m^2. This reduction is

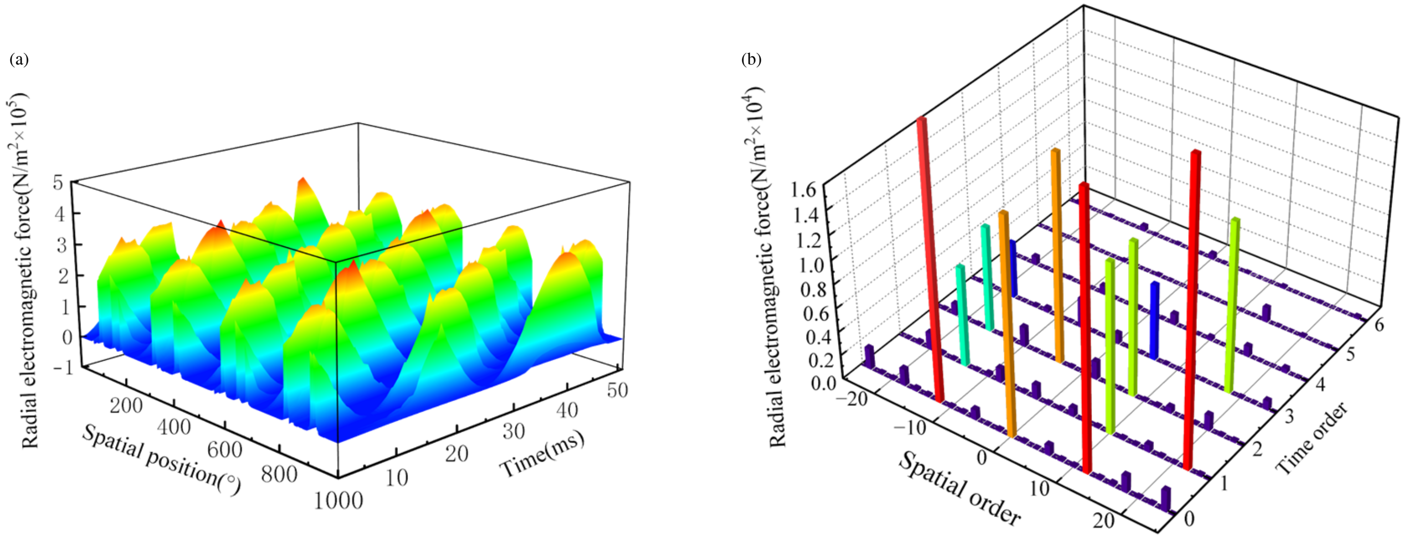

FIGURE 7. Radial EFD and space-time harmonics under armature reaction condition. (a) Radial EFD and (b) space-time harmonics (Amplitude scale: one order lower than no-load case).

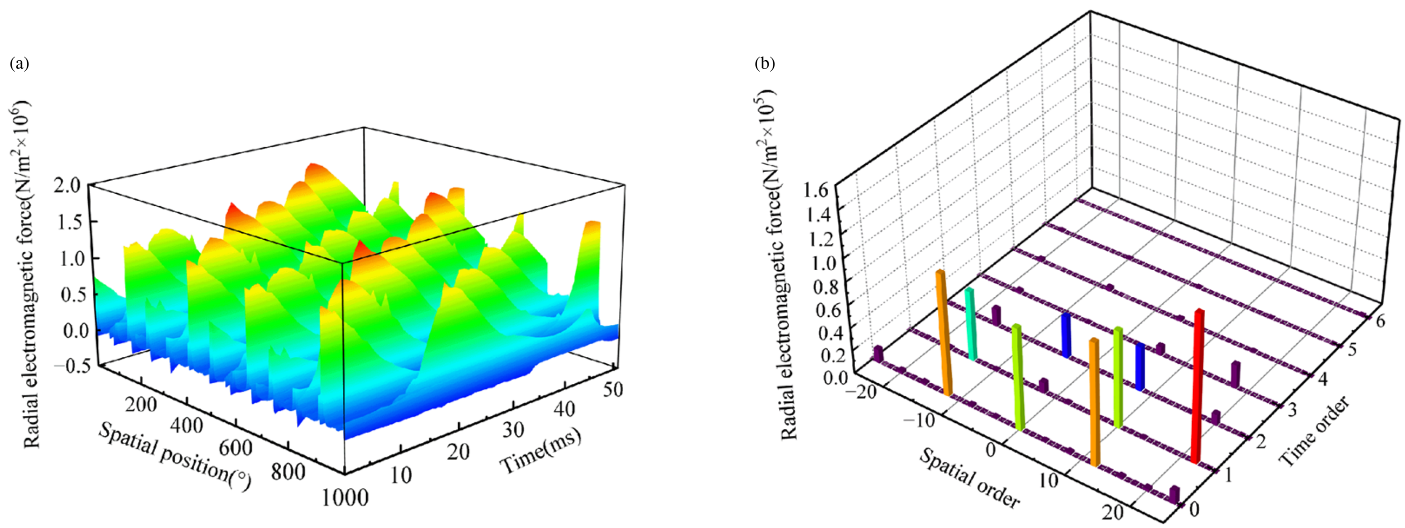

FIGURE 8. Radial EFD and space-time harmonics under load condition. (a) Radial EFD and (b) space-time harmonics.

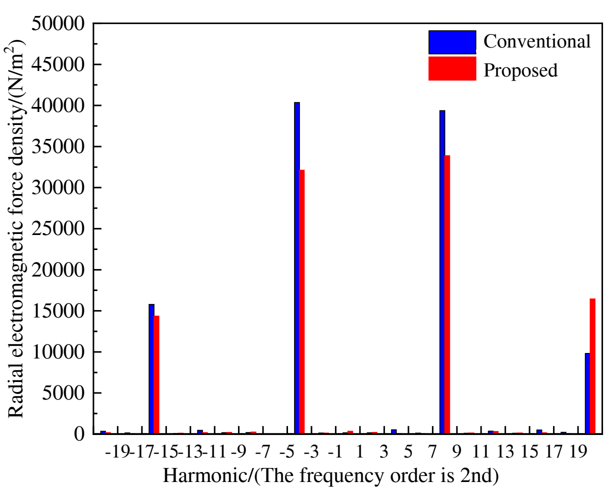

FIGURE 9. Comparison of radial EFD.

attributable to the U-shaped design, which optimizes air-gap flux distribution and suppresses harmonic amplitude, thus mitigating potential electromagnetic vibration.

Figure 10 compares the output torques of the proposed and conventional machines. In agreement with the no-load harmonic analysis, the dominant torque-producing harmonics of the proposed machine are all higher than those of the conventional machine. Although the 8th harmonic contributes negatively to the torque, the positive contributions from the other harmonic orders are substantially greater. Consequently, the proposed machine achieves a torque average of 26.16 N·m, which is 23.16% higher than that of the conventional machine. In addition, the torque ripple of the proposed machine is effectively reduced to 6.15%. A comprehensive comparison of the key electromagnetic performance is provided in Table 4.

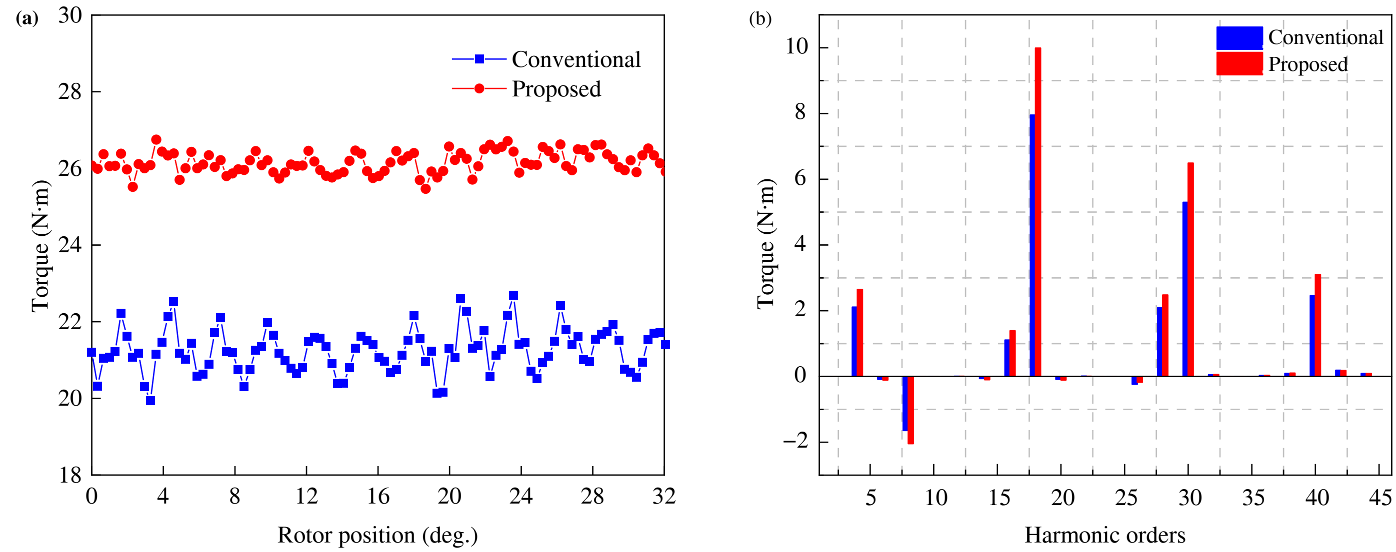

FIGURE 10. Output torque. (a) Waveform and (b) harmonic orders.

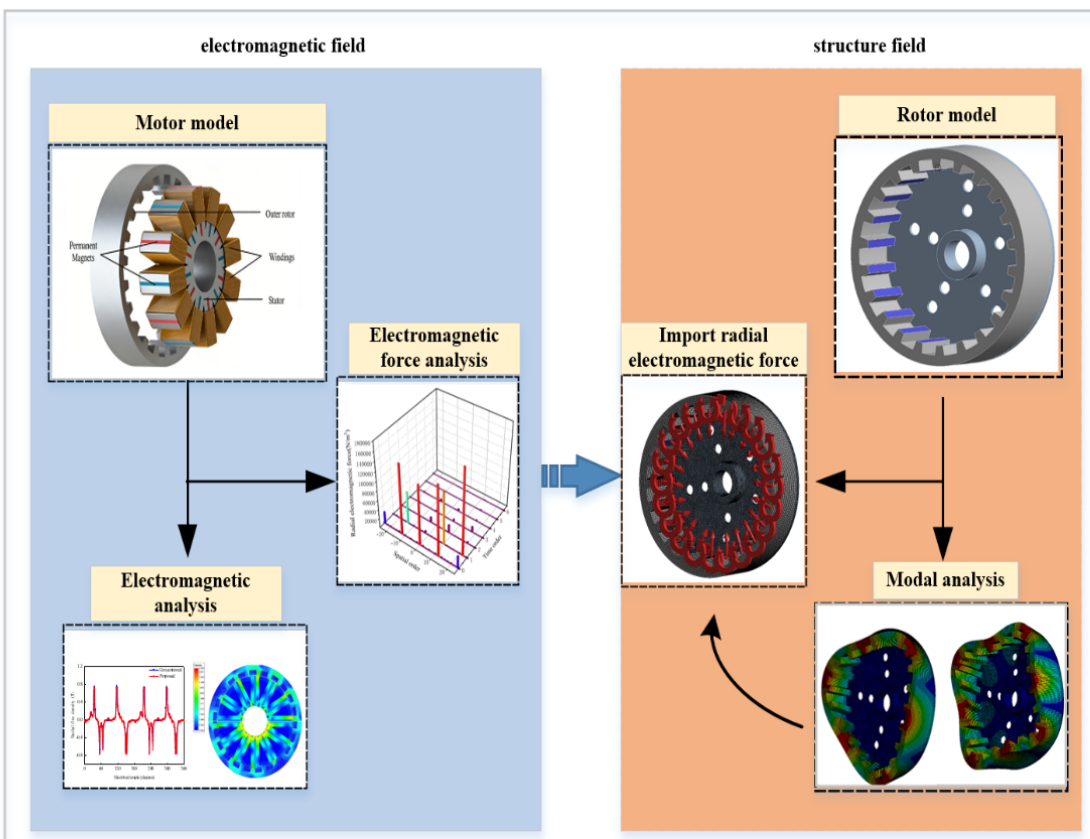

FIGURE 11. Vibration analysis process.

3. VIBRATION ANALYSIS

Machine vibrations stem from the interplay between electromagnetic forces and structural dynamics. Hence, accurate vibration prediction requires the knowledge of natural frequencies and mode shapes. The modal analysis procedure is illustrated in Fig. 11.

3.1. Modal Analysis of Outer Rotor

To account for the stiffening effect of end covers, the full rotor assembly is established to facilitate modal analysis. The material properties of modelled components are listed in Table 5.

A comparison of the first five natural frequencies of rotor assemblies with and without end covers is presented in Ta-

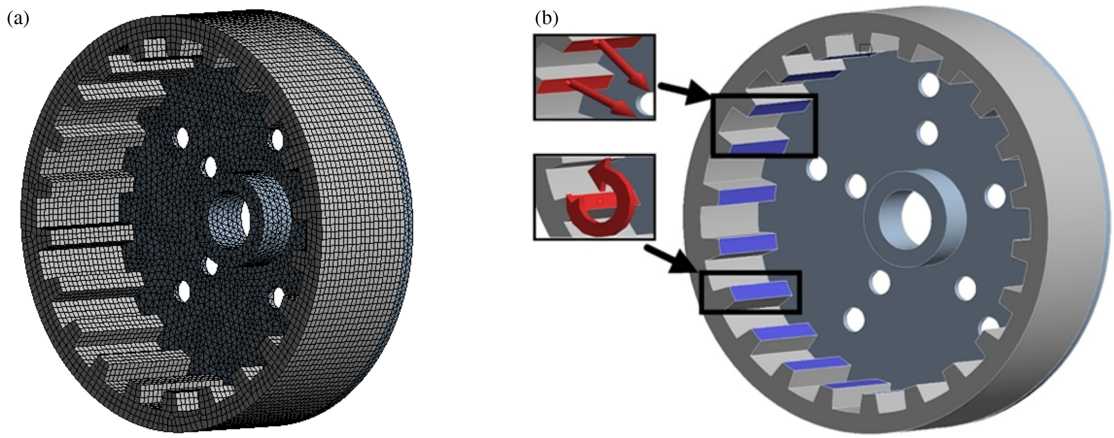

FIGURE 12. Rotor mesh and electromagnetic force loading.

TABLE 4. Electromagnetic performance comparison.

Parameter	Conventional machine	Proposed machine
PM volume (m^3)	9.39×10^{-5}	9.28×10^{-5}
Torque average (N·m)	21.24	26.16
Torque ripple	13.11%	6.15%
Output power (W)	1779.9	2191.8
Efficiency	90.21%	91.84%
Power factor	0.78	0.81
$(-4, 2f)$ EFD (N/m^2)	40358	32115
$(8, 2f)$ EFD (N/m^2)	39362	33881
$(14, 2f)$ EFD (N/m^2)	352.50	304.54

ble 6. As these low-order modes dominate the structural response within the principal excitation band, they are pivotal for vibration and noise evaluation. The results show that the addition of the end cover markedly redistributes the structural stiffness and elevates the second-order natural frequency, thereby widening the separation from the dominant electromagnetic excitation frequency.

3.2. Harmonic Response and Vibration Analysis

In Fig. 12, a hybrid mesh combining hexahedral and prism elements is adopted to balance accuracy and efficiency. The electromagnetic forces from the 2D field analysis are mapped as concentrated loads onto the rotor teeth via a node-based interpolation scheme that preserves total force and moment. The structural response is solved using modal superposition. Bearings are modeled as elastic supports; shaft ends are axially constrained with rotational freedom; and the rotor-shaft interface is treated as bonded contact with no slip.

The steady-state vibrational response is computed in the frequency domain via modal superposition, with the resulting acceleration spectra at selected rotor bore locations shown in Fig. 13. In the conventional machine, a 586.6 Hz electromagnetic harmonic coincides with the second flexural mode, producing a 7.65 m/s^2 acceleration peak and posing a clear resonant risk. In the proposed machine, this harmonic is reduced to 0.40 m/s^2, effectively mitigating the coincidence and ensuring a stable operating margin.

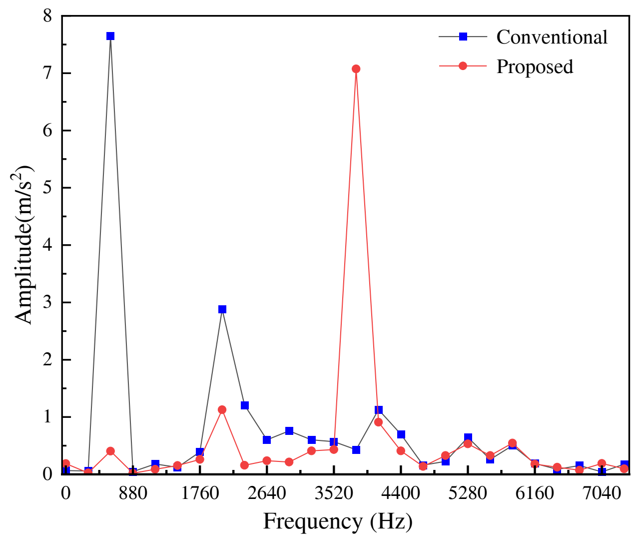

FIGURE 13. Vibration acceleration of rotor assembly.

Although a pronounced 14th-harmonic vibration acceleration appears in the proposed machine, the corresponding radial EFD amplitude is negligible. On the one hand, the small force magnitude is insufficient to excite a strong vibration response. On the other hand, this harmonic occurs at a relatively high frequency, where the structural mechanical impedance is large, thus naturally attenuating the vibration transmission. Consequently, this 14th-harmonic causes only a marginal increase in the overall vibration level.

Figure 14 compares the acoustic noise of the proposed and conventional machines. As can be observed, the proposed machine exhibits a significantly lower sound pressure level under rated operating conditions, with the dominant noise peak reduced from 86.9 dB in the conventional machine to 77.9 dB in the proposed design. This confirms that the U-shaped topology effectively mitigates both structural vibration and radiated acoustic noise.

TABLE 5. Material properties of OR-FSPM machine.

	End cover	Iron core	PM
Material	aluminum alloy	silicon steel sheet	neodymium iron boron
Young's modulus (GPa)	71	200	160
Poisson Ratio	0.33	0.3	0.25
Density (kg/m^3)	2700	7850	7600

TABLE 6. Modal frequency comparison of rotor components.

Modal order	No end cover	With end cover
2	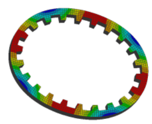 556.89 Hz	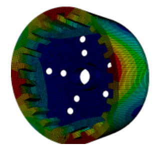 614.3 Hz
3	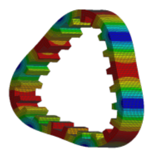 2050 Hz	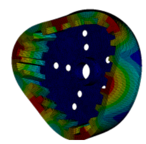 22449 Hz
4	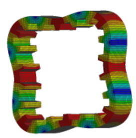 3858 Hz	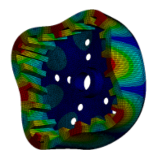 4011.8 Hz
5	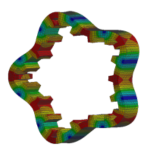 6101.9 Hz	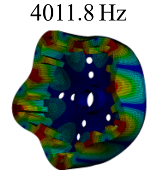 6334.5 Hz

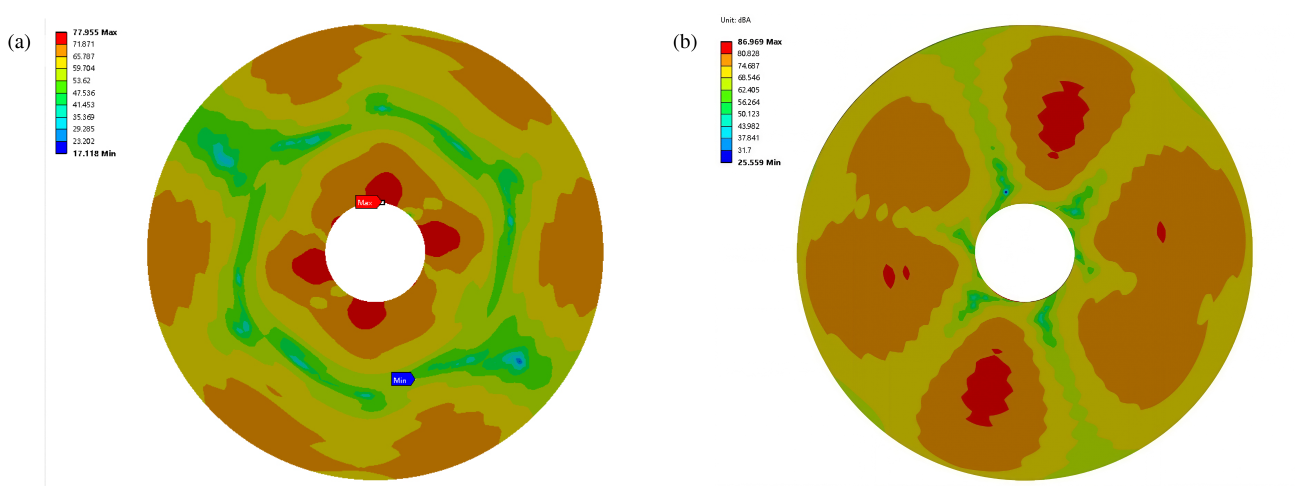

FIGURE 14. Acoustic noise analysis. (a) Proposed machine and (b) conventional machine.

4. CONCLUSION

In this study, the electromagnetic vibrational excitation mechanism in an OR-FSPM machine is analyzed. Using the magnetomotive force-permeance method and FE analysis, the main vibration source is determined to be a radial EFD harmonic with spatial order -4 and frequency $2f$. Harmonic response simulation shows that this harmonic excites the second-order mode, producing a 586.6-Hz resonant peak in the conventional machine. In the proposed machine, this dominant harmonic is reduced by approximately 20%, and the resonant acceleration drops from $7.65\,\mathrm{m/s^2}$ to $0.40\,\mathrm{m/s^2}$, indicating a lower resonant risk. Acoustic noise analysis further demonstrates that the radiated sound pressure level is also reduced, confirming the effectiveness of the proposed topology.

In future work, prototype manufacturing and experimental testing will be carried out to validate the simulation results. Additionally, a more comprehensive investigation under extended load and speed ranges will be conducted to further confirm the robustness and practical applicability of the proposed machine.

ACKNOWLEDGEMENT

This work was supported by the National Natural Science Foundation of China (52477056).

REFERENCES

[1] Husain, I., B. Ozpineci, M. S. Islam, E. Gurpinar, G.-J. Su, W. Yu, S. Chowdhury, L. Xue, D. Rahman, and R. Sahu, "Electric drive technology trends, challenges, and opportunities for future electric vehicles," *Proceedings of the IEEE*, Vol. 109, No. 6, 1039–1059, Jun. 2021.

[2] Thangavel, S., D. Mohanraj, T. Girijaprasanna, S. Raju, C. Dhanamjayulu, and S. M. Muyeen, "A comprehensive review on electric vehicle: Battery management system, charging station, traction motors," *IEEE Access*, Vol. 11, 20 994–21 019, 2023.

[3] Zhang, H., W. Hua, and G. Zhang, "Analysis of back-EMF waveform of a novel outer-rotor-permanent-magnet flux-switching machine," *IEEE Transactions on Magnetics*, Vol. 53, No. 6, 1–4, Jun. 2017.

[4] Abunike, C. E., O. I. Okoro, A. J. Far, and S. S. Aphale, "Advancements in flux switching machine optimization: Applications and future prospects," *IEEE Access*, Vol. 11, 110 910–110 942, 2023.

[5] Jiang, M., X. Zhu, Z. Xiang, L. Quan, H. Que, and B. Yu, "Suppression of torque ripple of a flux-switching permanent magnet motor in perspective of flux-modulation principle," *IEEE Trans. Transp. Electrif.*, Vol. 8, No. 1, 1116–1127, Mar. 2022.

[6] Jing, L. and Z. Min, "A novel flux-switching permanent magnet machine with dual sets of magnet arrangements," *J. of Electrical Engineering & Technology*, Vol. 18, No. 1, 299–306, 2023.

[7] Li, N., J. Li, D. Xu, X. Hao, Q. Li, and M. Lin, "Cogging torque minimization of axial flux-switching permanent magnet machine via rotor teeth skewing," in *2023 24th International Conference on the Computation of Electromagnetic Fields (COMPUMAG)*, 1–4, Kyoto, Japan, 2023.

[8] Lin, X., S. Fang, Q. Xu, and Z. Pan, "Detent torque analysis of multi-stator-module permanent magnet arc machine based on a hybrid analytical model considering asymmetric stator and rotor eccentricity," *IEEE Transactions on Energy Conversion*, Vol. 40, No. 4, 3175–3185, Dec. 2025.

[9] Yang, H., Y. Li, H. Lin, Z. Q. Zhu, and S. Lyu, "Principle investigation and performance comparison of consequent-pole switched flux PM machines," *IEEE Trans. Transp. Electrif.*, Vol. 7, No. 2, 766–778, Jun. 2021.

[10] Bi, Y., W. Fu, and S. Niu, "Quantitative analysis and comparison of in-wheel outer rotor consequent-pole flux-switching permanent magnet machines with different magnet arrangements," in *2023 IEEE International Magnetic Conference — Short Papers (INTERMAG Short Papers)*, 1–2, Sendai, Japan, 2023.

[11] Chen, H., X. Liu, N. A. O. Demerdash, A. M. El-Refaie, Z. Chen, and J. He, "Computationally efficient optimization of a five-phase flux-switching PM machine under different operating conditions," *IEEE Transactions on Vehicular Technology*, Vol. 68, No. 7, 6495–6508, Jul. 2019.

[12] Liu, W. and T. A. Lipo, "Analysis of consequent pole spoke type vernier permanent magnet machine with alternating flux barrier design," *IEEE Transactions on Industry Applications*, Vol. 54, No. 6, 5918–5929, Nov.–Dec. 2018.

[13] Bi, Y., W. Fu, S. Niu, X. Zhao, J. Huang, and Z. Qiao, "Torque enhancement of a dual-PM flux-switching machine with improved multiple high-order working harmonics," *IEEE Trans. Transp. Electrif.*, Vol. 10, No. 2, 2830–2843, Jun. 2024.

[14] Chen, C., X. Ren, D. Li, R. Qu, K. Liu, and T. Zou, "Torque performance enhancement of flux-switching permanent magnet machines with dual sets of magnet arrangements," *IEEE Trans. Transp. Electrif.*, Vol. 7, No. 4, 2623–2634, Dec. 2021.

[15] Qiao, Z., Y. Zhang, J. Luo, W. Fu, Y. Bi, and J. Huang, "Design and analysis of a consequent-pole flux switching permanent magnet machine with flux-concentrated magnet for torque enhancement," *IEEE Transactions on Energy Conversion*, Vol. 39, No. 4, 2468–2479, Dec. 2024.

[16] Min, Z., L. Jing, T. Wang, and R. Qu, "A partitioned stator flux switching PM machine with strongly coupled flux reversal effect," *IEEE Trans. Transp. Electrif.*, 2026.

[17] Zhu, X., W. Hua, and Z. Wu, "Cogging torque suppression in flux-reversal permanent magnet machines," *IET Electric Power Applications*, Vol. 12, No. 1, 135–143, Jan. 2018.

[18] Zhu, X. and W. Hua, "An improved configuration for cogging torque reduction in flux-reversal permanent magnet machines," *IEEE Transactions on Magnetics*, Vol. 53, No. 6, 1–4, Jun. 2017.

[19] Song, P., W. Li, Z. Li, and N. C. Kar, "Comparative analysis of noise and vibration for dual three-phase IPMSM under healthy and multi-phase open-circuit fault operations," *IEEE Transactions on Magnetics*, Vol. 59, No. 11, 1–7, Nov. 2023.

[20] Lu, Y., J. Li, R. Qu, D. Ye, H. Lu, J. Sun, M. Ge, and H. Xu, "Electromagnetic force and vibration analysis of permanent-magnet-assisted synchronous reluctance machines," *IEEE Transactions on Industry Applications*, Vol. 54, No. 5, 4246–4256, Sep.–Oct. 2018.

[21] Du, J., R. Zhong, Z. Wu, W. Hua, Z. Wu, H. Yin, and Y. Hu, "Analysis of dominant electromagnetic force harmonics in external-rotor SPM machine considering tangential force," *IEEE Transactions on Industrial Electronics*, Vol. 72, No. 9, 8860–8871, Sep. 2025.

[22] Kim, Y.-S., H.-K. Lee, J.-W. Yang, W.-S. Jung, Y.-T. Choi, J.-H. Jang, Y.-J. Kim, K.-H. Shin, and J.-Y. Choi, "Electromagnetic noise and vibration analyses in PMSMs: considering stator tooth modulation and magnetic force," *Electronics*, Vol. 14, No. 14, 2882, 2025.

[23] Fang, H., D. Li, R. Qu, J. Li, and D. Liang, "Vibration suppression for flux-switching PM machines," *IEEE Transactions on Energy Conversion*, Vol. 33, No. 3, 959–969, Sep. 2018.